minerals

MDPI

Article

Magma Source and Petrogenesis of the Early Cretaceous Granites in The Liaodong Peninsula: Evidence from In Situ Apatite Sr-Nd and Zircon Hf-O Isotopes

Miaomiao Linghu, Zimu Li, Jinfeng Sun * and Jiheng Zhang

Key Laboratory of Computational Geodynamics, University of Chinese Academy of Sciences, Beijing 100049, China; linghumiaomiao20@mails.ucas.ac.cn (M.L.); lizimu21@mails.ucas.ac.cn (Z.L.); zhjiheng@ucas.ac.cn (J.Z.)

* Correspondence: sjf@ucas.ac.cn

Abstract: Apatite Sr-Nd and zircon Hf-O isotopes are broadly used to trace magma sources and constrain magma evolution processes, further improving our understanding of the origin of granitoids. We present zircon U-Pb ages, whole-rock major and trace elements, and whole-rock Sr-Nd-Hf, zircon Hf-O, and apatite Sr-Nd isotopic data for the coarse-grained quartz monzonite, biotite monzogranite, and granite porphyry in the Yushulinzi pluton in the Liaodong Peninsula, the eastern North China Craton, to establish their magma sources and petrogenesis. The coarse-grained quartz monzonite, biotite monzogranite, and granite porphyry were formed contemporaneously, with zircon U-Pb ages of 123–119 Ma. They share enriched whole-rock Sr-Nd-Hf and zircon Hf isotopic compositions, and the coarse-grained quartz monzonite has crust-like $\delta^{18}O$ values (5.7–6.7‰). The coarse-grained quartz monzonite and biotite monzogranite have variable apatite $(^{87}Sr/^{86}Sr)_i$ ratios and negative apatite $\varepsilon_{Nd}(t)$ values. These isotopic characteristics indicate that the different rock types in the Yushulinzi pluton were derived from the partial melting of ancient crustal material in the North China Craton. Their geochemical and petrographic characteristics indicate that the crystal-melt segregation model can be employed to elucidate the genetic links among different rock types, with the coarse-grained quartz monzonite representing crystal accumulation and the biotite monzogranite and granite porphyry representing interstitial melts extracted from a crystal-rich magma chamber. Furthermore, the variable apatite Sr isotopic compositions and subtle differences in the peak zircon $\varepsilon_{Hf}(t)$ values of the studied rock samples confirm the possibility of a contribution from shallow crustal components and materials with high $\varepsilon_{Hf}(t)$ values during magma evolution, which is not readily revealed by their whole-rock Sr-Nd-Hf isotopic compositions. These results demonstrate that in situ apatite Sr-Nd and zircon Hf-O isotopic analyses have the potential to provide distinctive insights into the magma sources and evolution of magmatic systems.

Keywords: apatite; zircon; magma source; crystal-melt segregation; in situ isotopic analyses; Yushulinzi pluton; North China Craton

check for updates

Citation: Linghu, M.; Li, Z.; Sun, J.; Zhang, J. Magma Source and Petrogenesis of the Early Cretaceous Granites in The Liaodong Peninsula: Evidence from In Situ Apatite Sr-Nd and Zircon Hf-O Isotopes. *Minerals* **2023**, *13*, 545. https://doi.org/10.3390/min13040545

Academic Editor: Ioan Seghedi

Received: 28 February 2023
Revised: 6 April 2023
Accepted: 10 April 2023
Published: 12 April 2023

Copyright: © 2023 by the authors. Licensee MDPI, Basel, Switzerland. This article is an open access article distributed under the terms and conditions of the Creative Commons Attribution (CC BY) license (https://creativecommons.org/licenses/by/4.0/).

1. Introduction

Granitoids are significant building blocks of the continental crust as well as a symbol of the formation and evolution of the continents [1–7]. Therefore, the rock assemblages, magma sources, and petrogenesis of granites are enduring research subjects in geology, providing important information for investigating the formation and differentiation of the continental crust. Many studies have revealed that the formation of granites generally involves complex magmatic evolutionary processes, such as batch melting, magma mixing, crystal fractionation, and assimilation [8–11], resulting in changes in their original magma compositions; therefore, crystalized granites are hardly representative of the initial magma composition. Hence, identifying the nature of the primitive magma and effectively tracing the fine petrogenetic processes are central to current studies of granitoid petrogenesis nowadays.

Whole-rock geochemistry has been previously used to trace magmatic evolutionary processes and petrogenesis. However, whole-rock compositions are thought to be representative of the result of complex magma evolution, obscuring information about the complex magmatic evolution, whereas in situ accessory mineral geochemical analysis provides a crucial tool for elucidating magmatic evolution. In situ zircon trace element and Hf-O isotopic analyses have been widely applied in petrogenetic studies of granites to effectively trace the magma source and evolution processes, as well as the growth and evolution of the continental crust [12–18]. Additionally, with the advancement of analytical techniques, in situ accessory mineral isotopic analyses have advanced significantly in the research on magmatism, particularly Sr-Nd isotopes in apatite and titanite [19–24], which could provide exceptional insights for tracking the magmatic sources and petrogenesis of granites.

Recent studies have shown that during the Mesozoic, a loss of stability occurred in the eastern North China Craton (NCC), which has been defined as craton destruction or decratonization [25–28], triggering a great deal of shallow crustal responses, including large-scale magmatism [26,29,30], intensive tectonic activities [31–34], and mineralization [35–39]. Previous magmatic-tectonic geochronology studies have suggested that the Early Cretaceous was the peak period of the NCC destruction [27,33,36,37,40]. The Liaodong Peninsula, an area in which large-scale Early Cretaceous I-type and A-type granites and associated basalts and alkaline rocks are distributed, is located in the eastern segment of the NCC. The study area provides significant scientific materials for research on the magmatic sources and processes of granites and the evolution of the continental crust [8,29,41–45]. The Early Cretaceous Yushulinzi pluton in the Liaodong Peninsula was the focus of this study. Based on whole-rock geochemistry and zircon Hf-O and apatite Sr-Nd isotopic analyses, we traced the magma source and petrogenesis of the different rock types in the Yushulinzi pluton, aiming to contribute to the investigation of the evolution of the continental crust in the setting of the NCC destruction.

2. Geology and Petrology

2.1. Regional Geology

The Liaodong Peninsula has been found to contain the oldest rocks in China with U-Pb ages exceeding 3.8 Ga [46]. It is located in the eastern part of the NCC (Figure 1a) and is predominately composed of a series of Archean trondhjemite-tonalite-granodiorite rocks and Paleoproterozoic, lightly metamorphosed, sedimentary and volcanic rocks [47]. Compositionally, the Paleoproterozoic Liaohe group, which overlies the Archean metamorphosed rocks, consists mainly of schist, gneiss, marble, and amphibolite [48]. The Liaohe group was deposited and then metamorphosed for approximately 1.93 Ga, documenting the cratonization of the eastern NCC [49,50]. The Liaodong Peninsula was subsequently overlain by a thick succession dominated by Meso- to Neoproterozoic and Paleozoic sediments [30,51], suggesting a period of tectonic stability.

During the late Mesozoic, more than ~20,000 km^2 of intrusive rocks were widely developed in the Liaodong Peninsula. (Figure 1b) [26,29,30]. According to previous geochronology research, these intrusions could be categorized into three groups: (1) Triassic intrusions represented by two rock assemblages (alkaline rocks and dolerite-diorite-granite) [45,52–54]; (2) Jurassic intrusions (180–153 Ma) with rock assemblage comprising gneissic two-mica monzogranite, tonalite, and granodiorite, all of which have been subjected to varying degrees of deformation [26,30]; and (3) Early Cretaceous (131–120 Ma) intrusive rocks with little to no deformation, including diorite, quartz diorite, granodiorite, syenogranite, and monzogranite [26,29].

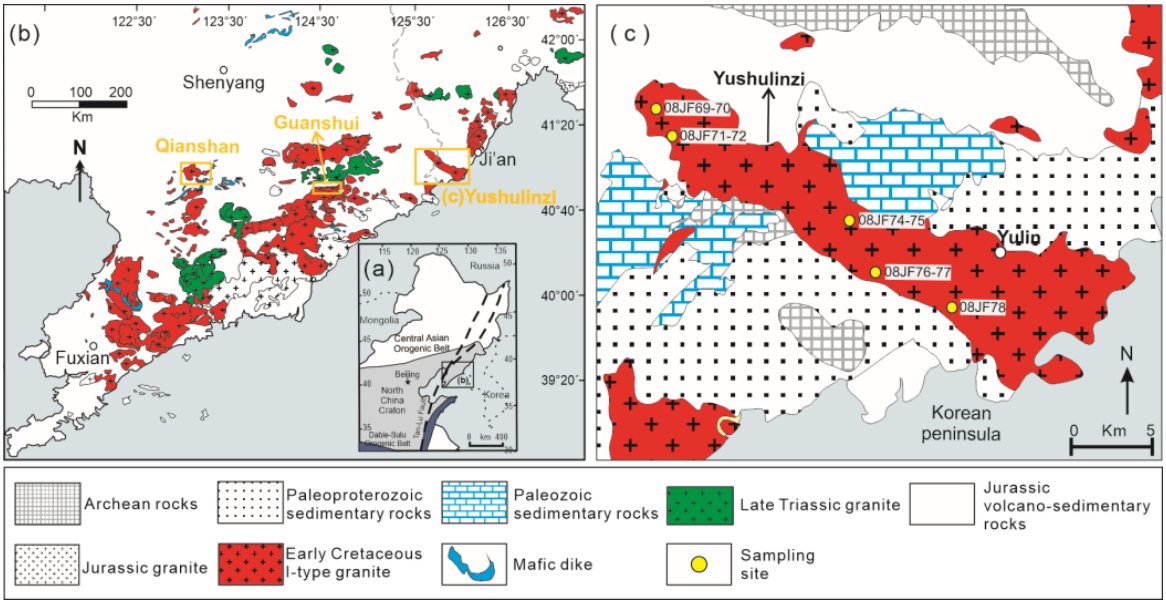


Figure 1. (**a**) Simplified geological map of eastern China; (**b**) Simplified geological map showing the location of the study area and the distributions of the Mesozoic intrusions in the Liaodong Peninsula; (**c**) Geological map of the Yushulinzi pluton showing the sample sites.

2.2. Yushulinzi Pluton

The Yushulinzi pluton is located in the northeastern part of the Liaodong Peninsula (Figure 1b). It is a NW-trending elongated intrusion with an outcrop area of ~105 km^2 and is controlled by a NW-striking fault. The Yushulinzi pluton intrudes into the Late Jurassic andesites of the Guosong Formation. The Yushulinzi pluton is mainly comprised of coarse-grained quartz monzonite, biotite monzogranite, and granite porphyry (Figure 2). Previous studies have reported the zircon U-Pb age of 123 Ma for the Yushulinzi pluton [55].

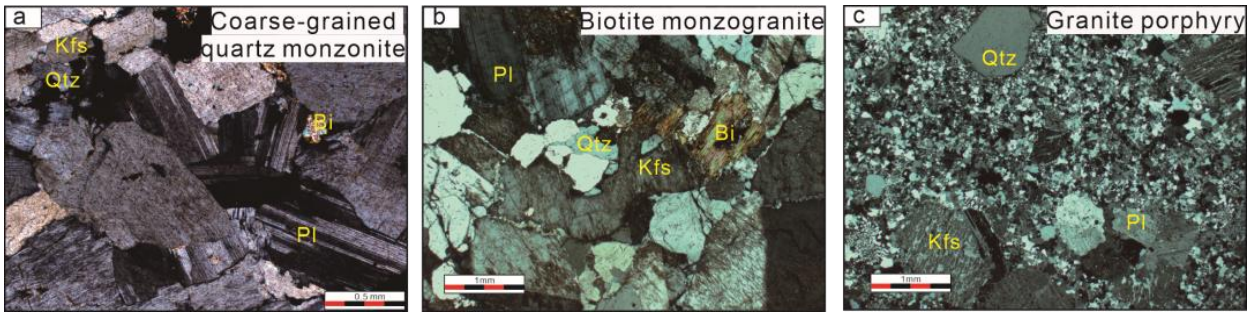


Figure 2. Major mineral assemblages of the (**a**) coarse-grained quartz monzonite, (**b**) biotite monzogranite, and (**c**) granite porphyry in the Yushulinzi pluton. Kfs, K-feldspar; Pl, plagioclase; Qtz, quartz; Bi, biotite.

The coarse-grained quartz monzonite (samples 08JF76–78) is characterized by a coarse-grained texture and massive structure. Its mineral assemblage mainly consists of subhedral plagioclase (~40%), subhedral K-feldspar (~35%), dark minerals (~15%), and minor anhedral quartz (~5%). Plagioclase developed polysynthetic twinning, and K-feldspar showed kaolinization (Figure 2a).

The biotite monzogranite (samples 08JF69, 74–75) is mainly comprised of subhedral K-feldspar (~35%), euhedral-subhedral plagioclase (~30%), anhedral quartz (~25%), and minor subhedral biotite (<5%) (Figure 2b). The biotite monzogranite has a medium-grained texture, granitic texture, and massive structure.

The mineral assemblages of the granite porphyry (samples 08JF70–72) principally include 1–3 mm long subhedral quartz (10–15%), subhedral-anhedral K-feldspar (~10%), and minor amounts of plagioclase (~5%). Of these, the K-feldspar, quartz, and plagioclase phenocrysts are set in a mineralogically similar fine-grained matrix (Figure 2c).

3. Analytical Methods

3.1. Whole-Rock Geochemical Analyses

3.1.1. Whole-Rock Major and Trace Element Analyses

The major element oxide concentrations were analyzed at the Institute of Geology and Geophysics, Chinese Academy of Sciences (IGGCAS), Beijing, China. The sample powders were mixed with a flux agent $Li_2B_4O_7$ + $LiBO_2$ to make glass disks for X-ray fluorescence (XRF) analysis. The analytical uncertainties of the element oxides were ~1% for contents of greater than 10 wt.% and ~5% for contents of less than 1 wt.%. The whole-rock trace element concentrations were determined using the Agilent 7700e Q-ICPMS instrument at the IGGCAS, Beijing, China. Rock standards BIR-1, BHVO-2, AGV-2, GSP-2, and RGM-1 were employed as external standards, and an internal standard Rh was also employed. For most of trace elements, the precision and accuracy of the analyses are generally better than 5%.

3.1.2. Whole-Rock Sr-Nd-Hf Isotopic Analyses

Whole-rock Rb-Sr, Sm-Nd, and Lu-Hf isotopic analyses were conducted on the Thermo Scientific Neptune multicollector inductively coupled plasma mass spectrometer (MC-ICP-MS) at the IGGCAS (Thermo Scientific, Waltham, MA, USA). The detailed analytical procedures have been summarized by Yang et al. [56,57]. The Sr, Nd, and Hf contents of the whole procedural blanks were <100 pg, <50 pg, and <50 pg, respectively. The $^{87}Sr/^{86}Sr$, $^{143}Nd/^{144}Nd$, and $^{176}Hf/^{177}Hf$ ratios were calibrated to $^{86}Sr/^{88}Sr$ = 0.1194, $^{146}Nd/^{144}Nd$ = 0.7219, and $^{179}Hf/^{177}Hf$ = 0.7325, respectively, using the corresponding exponential law. The values of the standards measured were $^{87}Sr/^{86}Sr$ = 0.710250 ± 0.000009 (2σ, n = 9) for NBS987, $^{143}Nd/^{144}Nd$ = 0.512109 ± 0.000002 (2σ, n = 5) for JNdi-1, and $^{176}Hf/^{177}Hf$ = 0.282182 ± 0.000003 (2σ, n = 7) for Alfa Hf 14374. Additionally, rock standards RGM-1, GSP-2, AGV-2, and BIR-1 were processed for Sr-Nd-Hf isotopic analyses, yielding $^{87}Sr/^{86}Sr$ ratios of 0.704257 ± 0.000016 (2σ), 0.764996 ± 0.000019 (2σ), 0.703959 ± 0.000015 (2σ), and 0.703117 ± 0.000029 (2σ); $^{143}Nd/^{144}Nd$ ratios of 0.512793 ± 0.000004 (2σ), 0.511361 ± 0.000004 (2σ), 0.512789 ± 0.000008 (2σ), and 0.513102 ± 0.000013 (2σ); and $^{176}Hf/^{177}Hf$ ratios of 0.283005 ± 0.000008 (2σ), 0.281931 ± 0.000006 (2σ), 0.282964 ± 0.000008 (2σ), and 0.283221 ± 0.000029 (2σ), respectively, which are in agreement with their recommended values within the error ranges [58–60].

3.2. In Situ Zircon Analyses

The in situ laser ablation inductively coupled plasma mass spectrometry (LA-ICP-MS) and second ion mass spectrometry (SIMS) zircon U-Pb age measurements and Hf-O isotopic analyses were performed at the IGGCAS. Cathodoluminescence (CL) images of the zircon grains and backscattered-electron (BSE) images of the apatite grains were obtained using the JXA-8100 electron microscope at the IGGCAS to characterize the internal structures of the zircon and apatite grains.

3.2.1. Zircon U-Pb Dating and O-Isotope Measurements via SIMS

The in situ U-Pb ages and O isotope compositions of the zircon grains were measured using a CAMECA IMS-1280 ion microprobe. The analytical techniques, instrumental conditions, and data processing procedures for the SIMS zircon U-Pb dating and O-isotope analyses were similar to those described by Li et al. [61,62]. The U-Th-Pb isotopic compositions and absolute abundances were calculated against standard zircon TEMORA (417 Ma) [63]. The measured ^{204}Pb values were applied to calibrate for the common Pb. Standard zircon Qinghu was analyzed as an unknown sample, yielding a weighted average $^{206}Pb/^{238}U$ age of 161.0 ± 2.0 Ma (2σ, n = 6), which is identical to its recommended values

of 159.5 ± 0.2 Ma within the analytical error [61]. Data reduction was performed using Isoplot/Ex version 3.0 [64]. The uncertainties of the individual measured results in the supplementary tables are reported at the 1σ level, and mean ages for the pooled U-Pb analyses are quoted at the 95% confidence interval. All of the obtained $^{18}O/^{16}O$ ratios were normalized to Vienna Standard Mean Ocean Water (VSMOW, $^{18}O/^{16}O = 0.0020052$). The correction for the instrumental mass fractionation (IMF) was performed using standard zircon TEMORA with a $\delta^{18}O$ value of 8.2‰. Standard zircon Qinghu was analyzed as an unknown, along with the unknown zircons, to evaluate the external uncertainties during the oxygen isotope measurements, yielding $\delta^{18}O$ values of 5.2‰ ± 0.5‰, which is consistent with its recommended value (5.39‰ ± 0.22‰) [65]. The long-term precision for the SIMS zircon O isotope measurements conducted in the laboratory was generally 0.5‰.

3.2.2. Zircon U-Pb Dating and Hf-Isotope Measurements Using LA-ICP-MS

The in situ zircon LA-ICP-MS U-Pb dating and Hf isotopic analyses were conducted using an Agilent 7500a quadrupole ICP-MS (Q-ICP-MS) and a Thermo Scientific Neptune MC-ICP-MS, respectively, both of which were equipped with a 193 nm ArF excimer laser ablation system. The details of the analytical methods and operation procedures for the zircon U-Pb dating and Hf isotopic analyses have been described by Xie et al. [66] and Wu et al. [67], respectively. Reference zircons 91500 and GJ-1 were chosen as standards to correct for U-Pb fractionation and to monitor the external uncertainties, respectively, and glass NIST 610 was used as an external calibration standard for the U, Th, and Pb concentration analyses. In the zircon U-Pb age analyses, the common Pb was calibrated using the method proposed by Andersen [68]. The data treatment was conducted using GLITTER version 4.0 [69]. The concordia diagrams and U-Pb age calculations were conducted using Isoplot/Ex v. 3.0 [64]. During the in situ zircon Hf-isotope analysis, zircon standards 91500 and GJ-1 were measured as the external standards to monitor the instrumental drift and for data correction. These standards yielded $^{176}Hf/^{177}Hf$ ratios of 0.282301 ± 0.000034 (2σ, n = 298) and 0.282023 ± 0.000044 (2σ, n = 149), which are close to their reference values of 0.282305 ± 0.000008 (2σ, n = 11) and 0.281999 ± 0.000008 (2σ, n = 10), respectively [70,71].

3.3. In Situ Sr and Nd Isotopic Analyses of Apatite

In situ Sr and Nd isotopic analyses of apatite were conducted using the Thermo Scientific Neptune MC-ICP-MS, equipped with a 193 nm excimer ArF laser-ablation system at the IGGCAS. The instrumental operation and analytical protocols have been described in detail in previous studies [21,72–74].

For the Sr isotopic analysis, a spot size of 80–100 μm, a laser repetition rate of 8 Hz, and an energy density of 15 J/cm^2 were applied. The analyses contained 30 s for correction of the background Kr, 40 s for sample data acquisition, and 60 s for cleaning. The interference of ^{87}Rb with ^{87}Sr was calibrated using the natural $^{85}Rb/^{87}Rb$ ratio of 2.593 [74]. The $^{87}Sr/^{86}Sr$ ratios obtained for reference material Durango and in-house standard apatite AP2 were 0.706353 ± 0.000020 (2σ, n = 19) and 0.706517 ± 0.000017 (2σ, n = 15), respectively, which are in good agreement with their reference values obtained via solution methods and long-term LA-MC-ICP-MS measurements [72,73].

For the Nd isotopic analysis, an energy density of 15 J/cm^2, a laser repetition rate of 8 Hz, and a spot size of 80–100 μm were employed. The interference of ^{142}Ce with ^{142}Nd was negligible due to the low Ce/Nd ratios of natural minerals, making the interference of ^{144}Sm with ^{144}Nd the primary isobaric interference in the apatite Nd isotopic analysis, which was calibrated using the method proposed by McFarlane et al. [75]. The $^{147}Sm/^{144}Nd$ and $^{143}Nd/^{144}Nd$ isotope ratios obtained for in-house reference materials AP1 and AP2 were 0.0849 ± 0.0005 (2σ, n = 31) and 0.511329 ± 0.000005 (2σ, n = 31) and 0.0782 ± 0.0002 (2σ, n = 68) and 0.510993 ± 0.000003 (2σ, n = 68), respectively, which are consistent with their recommended values obtained via solution methods and the long-term values measured in the laboratory [21,74].

4. Analytical Results

4.1. Zircon U-Pb Ages

Two coarse-grained quartz monzonites (08JF76 and 78), two biotite monzogranites (08JF69 and 74), and one granite porphyry (08JF71) samples from the Yushulinzi pluton were selected for zircon U-Pb dating via LA-ICP-MS and SIMS. Representative cathodoluminescence images of the selected zircon grains and the U-Pb concordia diagrams are presented in Figures 3 and 4, respectively. The detailed U-Pb results are summarized in Tables S1 and S2.

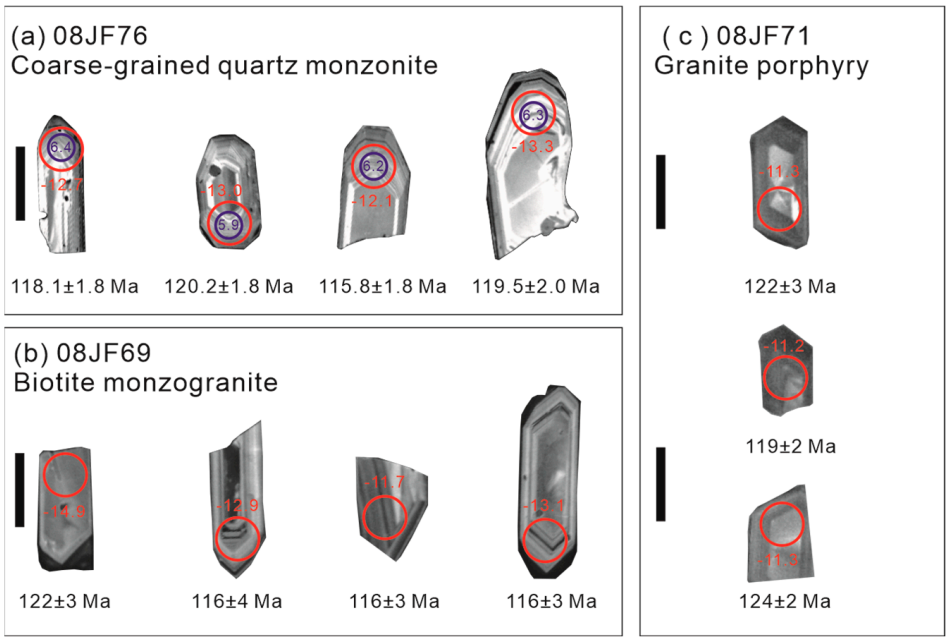


Figure 3. Representative cathodoluminescence (CL) images of zircons from the (**a**) coarse-grained quartz monzonite, (**b**) biotite monzogranite, and (**c**) granite porphyry in the Yushulinzi pluton. The blue circles represent the sites of the O isotopic analysis and the subsequent U-Pb dating analysis via SIMS. The red circles represent the locations of the U-Pb age analyses and the subsequent Hf isotope measurements via LA-(MC)-ICPMS. The scale bars in all of the CL images are 100 μm in length. The U-Pb age and $\delta^{18}O$ and $\varepsilon_{Hf}(t)$ values of the zircons are noted for each analytical grain.

The CL images show that the zircons extracted from the coarse-grained quartz monzogranite are euhedral prismatic crystals with lengths of greater than 100 μm, and they exhibit evident oscillatory zoning (Figure 3a). These zircon grains have high Th/U ratios of 0.7–1.8, suggesting a magmatic origin. The U-Pb age of sample 08JF76 (coarse-grained monzogranite) was determined using the zircon SIMS U-Pb method. Twenty analyses of zircons formed yielded a weighted mean $^{206}Pb/^{238}U$ age of 119.8 ± 0.9 Ma (2σ, n = 20) (Figure 4a). Sample 08JF78 was dated using the zircon LA-ICP-MS U-Pb method, and sixteen analyses of zircons yielded a weighted mean $^{206}Pb/^{238}U$ age of 120.7 ± 1.4 Ma (2σ, n = 16) (Figure 4b). This is virtually coeval with the U-Pb age of 119.8 ± 0.9 Ma (2σ, n = 20) for sample 08JF76 within the errors, so they both provide the best approximation of the crystallization age of the coarse-grained quartz monzogranite.

The CL images reveal that the zircons from the biotite monzogranite are long prismatic crystals with length/width ratios of 2:1 to 3:1 (Figure 3b), and they exhibit typical oscillatory zoning. They have Th/U ratios of 0.6–1.4. Weighted average $^{206}Pb/^{238}U$ ages of 119.0 ± 1.4 Ma (2σ, n = 17) (Figure 4c) and 121.6 ± 1.2 Ma (2σ, n = 17) (Figure 4d) were obtained for samples 08JF69 and 08JF74, respectively, via LA-ICP-MS zircon U-Pb dating. These ages are virtually identical within the analytical errors and represent the emplacement age of the biotite monzogranite.

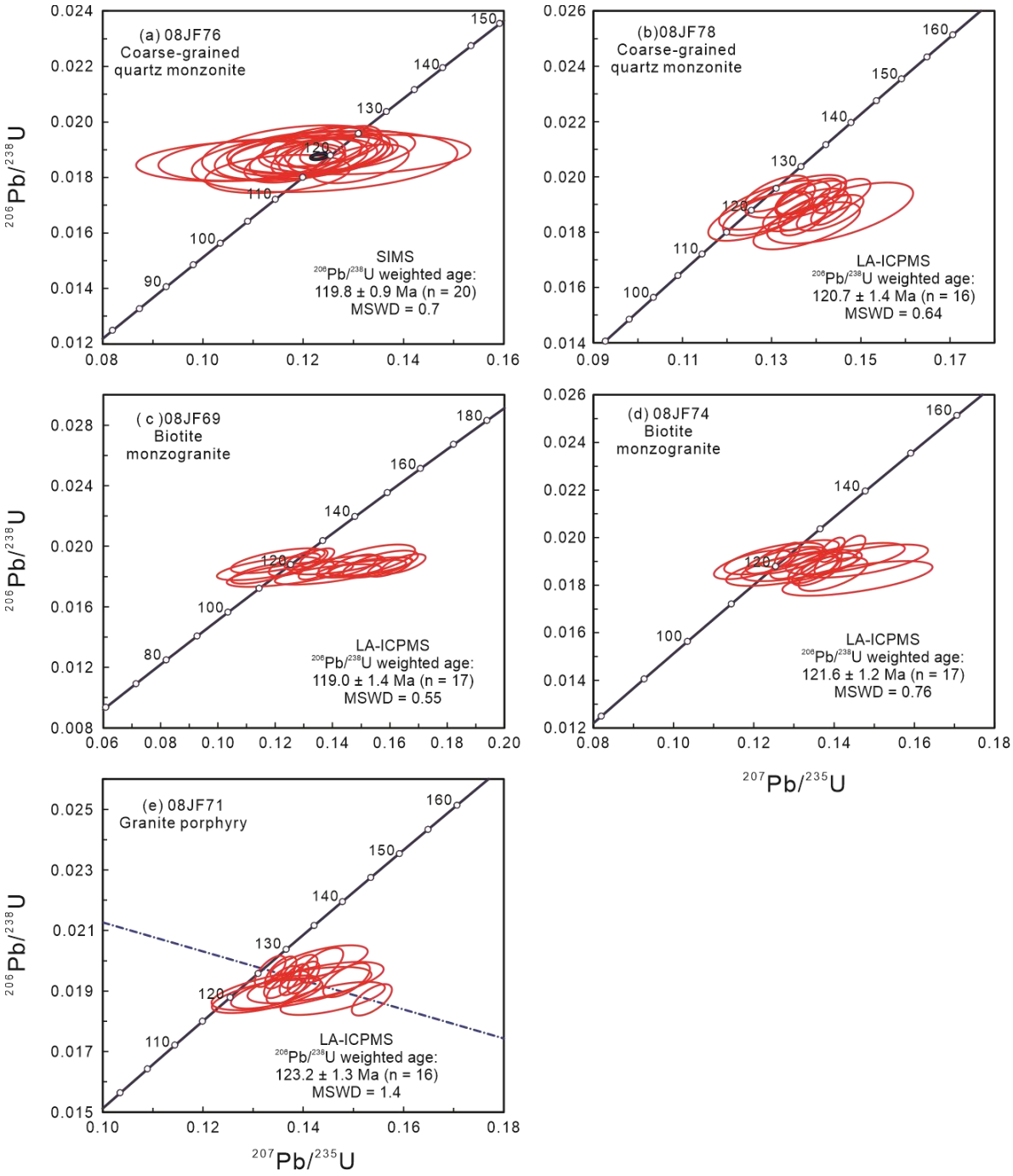


Figure 4. Concordia diagrams of the zircon U-Pb age data obtained via the SIMS and LA-ICP-MS methods for the (**a**,**b**) coarse-grained quartz monzonite, (**c**,**d**) biotite monzogranite, and (**e**) granite porphyry in the Yushulinzi pluton. The analytical technique, weighted average age, and MSWD are reported.

The CL images show that the zircons from the granite porphyry (08JF71) are short prismatic crystals (Figure 3c), and they have Th/U ratios of 0.4–1.1. Sixteen analyses of zircons dated using the LA-ICP-MS zircon U-Pb method yielded a weighted mean $^{206}Pb/^{238}U$ age of 123.2 ± 1.3 Ma (2σ, *n* = 16) (Figure 4e), which is interpreted as the age of crystallization for the granite porphyry.

In summary, the coarse-grained quartz monzogranite, biotite monzogranite, and granite porphyry in the Yushulinzi pluton were all formed during the Early Cretaceous and have consistent zircon U-Pb ages within errors, indicating coeval magmatic activities.

4.2. Whole-Rock Major and Trace Element and Sr-Nd-Hf Isotopic Compositions

Nine fresh rock samples, comprising three coarse-grained quartz monzonites, three biotite monzogranites, and three granite porphyries, were selected for whole-rock geochemical analysis. The results of whole-rock major and trace element analyses are plotted in Figures 5–7 and are summarized in Table S3, and whole-rock Sr-Nd-Hf isotopic compositions are presented in Table S4.

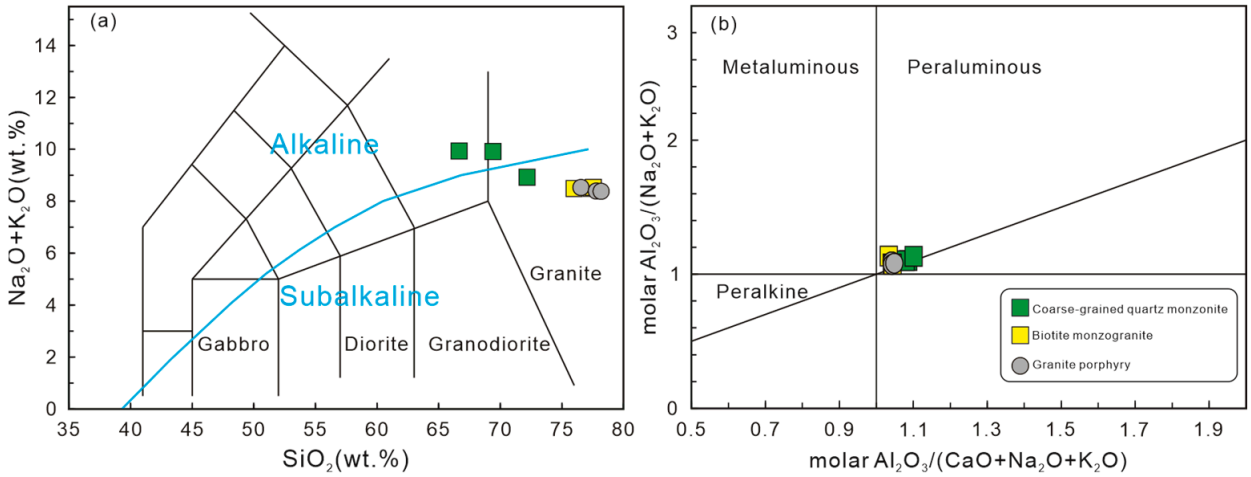


Figure 5. Diagrams of (**a**) $Na_2O + K_2O$ vs. SiO_2 (TAS) and (**b**) A/NK [molar ratio $Al_2O_3/(Na_2O + K_2O)$] vs. A/CNK [molar ratio $Al_2O_3/(CaO + Na_2O + K_2O)$] for the coarse-grained quartz monzonite, biotite monzogranite, and granite porphyry samples from the Yushulinzi pluton in the Liaodong Peninsula.

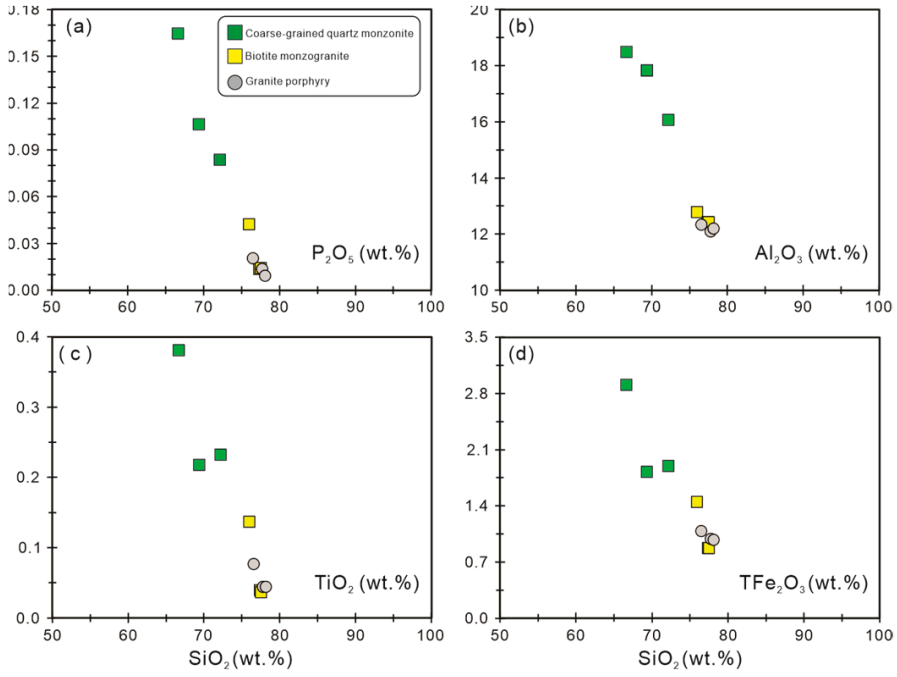


Figure 6. Diagrams of SiO_2 versus (**a**) P_2O_5, (**b**) Al_2O_3, (**c**) TiO_2, and (**d**) TFe_2O_3 for the coarse-grained quartz monzonite, biotite monzogranite, and granite porphyry samples from the Yushulinzi pluton in the Liaodong Peninsula.

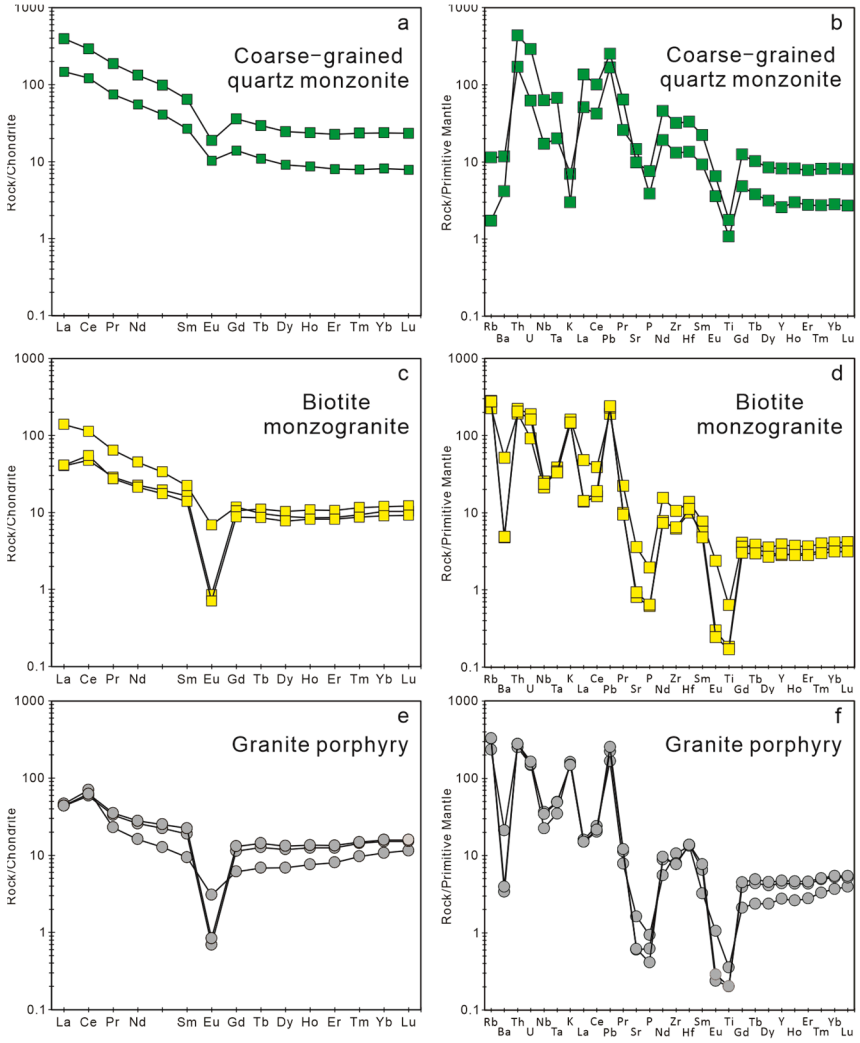


Figure 7. Chondrite-normalized REE patterns (**a**,**c**,**e**) and primitive mantle (PM)-normalized trace element spider diagrams (**b**,**d**,**f**) for the coarse-grained quartz monzonite, biotite monzogranite, and granite porphyry in the Yushulinzi pluton in the Liaodong Peninsula. The chondrite and primitive mantle values are from Sun et al. [76].

On the total alkalis versus SiO_2 (TAS) diagram (Figure 5a), all of the samples from the Yushulinzi pluton plot in the syenite and granite fields, which is virtually compatible with the petrographic observations. The different rock types in the Yushulinzi pluton have consistent total alkali (8.9–9.9 wt.%) contents (Table S3). The A/NK (molar ratio $Al_2O_3/(Na_2O + K_2O)$) vs. A/CNK (molar ratio $Al_2O_3/(CaO + Na_2O + K_2O)$) diagram shows that all of the samples plot in the peraluminous field (Figure 5b). The biotite monzogranite (08JF69, 74, and 75) has major element characteristics similar to those of the granite porphyry (08JF70–72) (Figure 6 and Table S3), with high SiO_2 (76.0–78.2 wt.%) and K_2O (4.4–4.9 wt.%) contents, and low TFe_2O_3 (0.9–1.5 wt.%), MgO (<0.3%), CaO (0.2–0.6 wt.%), MnO (<0.1 wt.%), Al_2O_3 (12.1–12.8 wt.%), and Na_2O (3.6–4.1 wt.%) contents. The coarse-grained quartz monzonite (08JF76–78) has distinctly different major element compositions from the aforementioned samples, with relatively low SiO_2 (66.7–72.2 wt.%), CaO (0.1–0.3 wt.%), and K_2O (0.1–0.2 wt.%) contents, and relatively high TFe_2O_3 (1.8–2.9 wt.%), Al_2O_3 (16.1–18.5 wt.%) and Na_2O (8.7–9.8 wt.%) contents (Figure 6).

The biotite monzogranite (08JF69, 74–75) and granite porphyry (08JF70–72) have similar concave-downward, chondrite-normalized, rare earth element (REE) patterns with relatively flat slopes (Figure 7c,e), which are characterized by low fractionation of light rare earth elements (LREEs) over heavy rare earth elements (HREEs) and significant negative

Eu anomalies. These samples have narrow total REE content ranges of 65–142 ppm. The biotite monzogranite and granite porphyry exhibit large ion lithophile element (LILE) enrichment (i.e., Rb, U, Th, and K) and pronounced Sr, Ti, and P depletions. The primitive mantle-normalized trace element spider diagrams reveal that both the biotite monzogranite and granite porphyry have negative Ba, Nb, Ta, Sr, P, Eu, and Ti anomalies and positive Rb and K anomalies (Figure 7d,f). In contrast, the coarse-grained quartz monzonite (08JF76–78) is characterized by a relatively wide range of total REE contents (156–386 ppm) and moderate $(La/Yb)_N$ values of 17–18. The chondrite-normalized REE diagram (Figure 7a) is characterized by a right-inclined slope from LREE to HREE and weak negative Eu anomalies. The primitive mantle-normalized trace element spider diagrams of the coarse-grained quartz monzonite samples exhibit distinct negative Rb, Ba, K, P, and Ti anomalies and positive Th, U, La, Ce, Zr, and Hf anomalies (Figure 7b).

The whole-rock Sr-Nd-Hf isotopic compositions of the coarse-grained quartz monzonite, biotite monzogranite, and granite porphyry samples from the Yushulinzi pluton are listed in Table S4. The coarse-grained quartz monzonite (08JF76 and 78) has extremely low $^{87}Rb/^{86}Sr$ ratios (<0.1) and relatively high initial $^{87}Sr/^{86}Sr$ ratios of 0.71413–0.71951. The biotite monzogranite (08JF69) has a low $^{87}Rb/^{86}Sr$ ratio (~5) and an initial $^{87}Sr/^{86}Sr$ ratio of 0.70824. Sample 08JF71 (granite porphyry) and sample 08JF74 (biotite monzogranite) have high $^{87}Rb/^{86}Sr$ ratios of 47.3 and 30.3, respectively, which were corrected to obtain initial $^{87}Sr/^{86}Sr$ ratios of 0.69954 and 0.70462, respectively (Table S4). The whole-rock $\varepsilon_{Nd}(t)$ values of different rock types fall within a restricted range of −12.4 to −11.4, with corresponding single-stage Nd model ages of 1512 to 2629 Ma. The whole-rock $\varepsilon_{Hf}(t)$ values of different rock types range from −13.1 to −12.4, with single-stage Hf model ages of 1487 to 1895 Ma (Table S4).

4.3. Zircon Hf-O Isotopes

The in situ zircon Hf isotopic data for the coarse-grained quartz monzonite, biotite monzogranite, and granite porphyry are plotted in Figure 8 and summarized in Table S5. The in situ O isotope data for one coarse-grained quartz monzonite (sample 08JF76) sample are listed in Table S5.

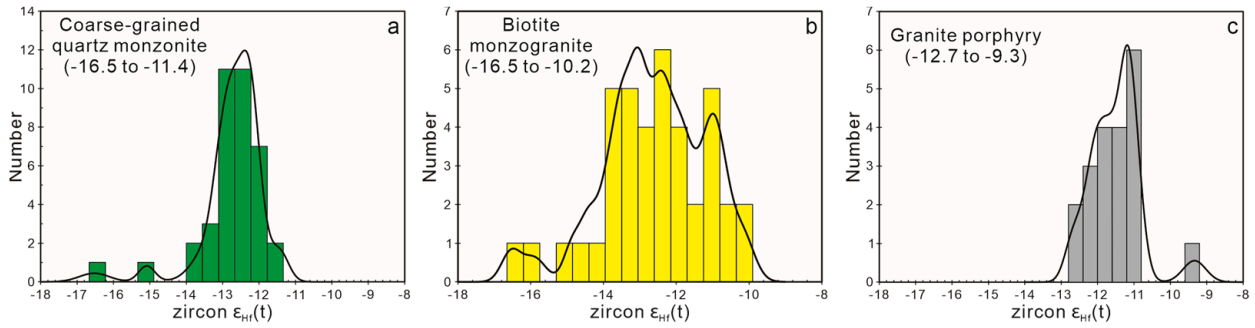


Figure 8. Histograms of the zircon $\varepsilon_{Hf}(t)$ values of the (**a**) coarse-grained quartz monzonite, (**b**) biotite monzogranite, and (**c**) granite porphyry in the Yushulinzi pluton in the Liaodong Peninsula.

The zircon $^{176}Hf/^{177}Hf$ ratios of the coarse-grained quartz monzonite (08JF76 and 78), biotite monzogranites (08JF69 and 74), and granite porphyry (08JF76) in the Yushulinzi pluton are 0.282238–0.282379, 0.282233–0.282416, and 0.282342–0.282440, respectively, which are consistent within the analytical errors, and their corresponding $\varepsilon_{Hf}(t)$ values and Hf model ages are generally consistent as well (Figure 8). The zircon grains extracted from the samples of different rock types have $\varepsilon_{Hf}(t)$ values of −16.5 to −9.3, with corresponding single-stage Hf model ages (T_{DM}) of 1232–1529 Ma and two-stage Hf model ages (T_{2DM}) of 2456–3098 Ma (Table S5). The coarse-grained quartz monzonite has $\delta^{18}O$ values of 5.7–6.7‰ (Table S5).

4.4. Sr-Nd Isotopic Compositions of Apatite

The in situ apatite Sr-Nd isotopic compositions of the coarse-grained quartz monzonite and biotite monzogranite are presented in Figure 9 and summarized in Table S6. The apatite grains analyzed in this study have variable $^{87}Rb/^{86}Sr$ ratios (0.003–0.095); however, the $^{87}Sr/^{86}Sr$ ratios of all of the studied apatite grains barely vary with their $^{87}Rb/^{86}Sr$ ratios, which demonstrates the reliability of the results of the in situ apatite Sr isotopic analysis (Table S6). The apatite grains from the coarse-grained quartz monzonite and biotite monzogranite have initial $^{87}Sr/^{86}Sr$ ratios of 0.70960–0.71577 and 0.70945–0.71321, respectively, which are not significantly different within the error ranges. In addition, they have homogeneous $\varepsilon_{Nd}(t)$ values of −13.3 to −10.5 and −12.9 to −10.7, respectively (Figure 9). Notably, the in situ Sr isotopic compositions of the apatite grains from the coarse-grained quartz monzonite and biotite monzogranite are significantly distinct from the whole-rock Sr isotopic compositions of their host rocks, whereas the in situ apatite Nd isotopic compositions are roughly identical to the whole-rock Nd isotopic compositions.

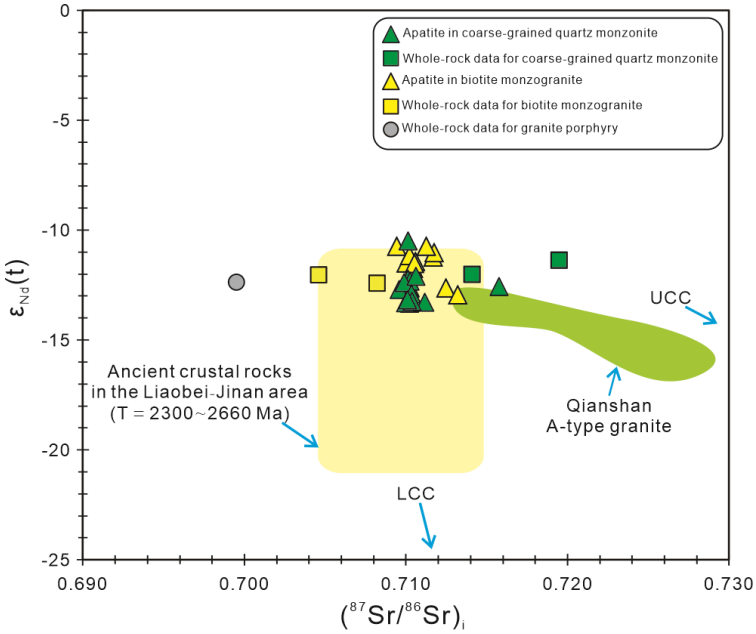


Figure 9. Plot of $\varepsilon_{Nd}(t)$ vs. $(^{87}Sr/^{86}Sr)_i$ for apatite grains extracted from the coarse-grained quartz monzonite and biotite monzogranite in the Yushulinzi pluton. The green and yellow squares and a gray circle represent the whole-rock Sr-Nd isotopic compositions of the coarse-grained quartz monzonite, biotite monzogranite, and granite porphyry, respectively. The data for the upper continental crust (UCC) and lower continental crust (LCC) are from [8,44,77]. The data for Qianshan A-type granites are quoted from Yang et al. [44]. The data for the ancient crustal rocks in the Liaobei-Jinan area are from [30,78,79].

5. Discussion

5.1. Magma Source and Petrogenesis

Comprehensive whole-rock major and trace element, whole-rock Sr-Nd-Hf, zircon Hf-O, and apatite Sr-Nd isotope analyses were performed to establish the magma source and petrogenesis of the Yushulinzi pluton, which is mainly composed of the coarse-grained quartz monzonite, biotite monzogranite, and granite porphyry.

On the Harker diagrams (Figure 6), the different rock types exhibit inverse correlations between P_2O_5, Al_2O_3, TiO_2, and TFe_2O_3 and SiO_2. The result of the whole-rock Sr-Nd-Hf and in situ apatite Sr-Nd isotopic analyses show that the different rock types have similar Nd-Hf isotopic compositions and variations, even though the Sr isotopic compositions of the studied samples vary considerably (Figure 9). In addition, the coarse-grained quartz monzonite, biotite monzogranite, and granite porphyry have consistent zircon $\varepsilon_{Hf}(t)$

ranges of −16.5 to −11.4, −16.5 to −10.2, and −12.7 to −9.3, respectively. Given that Sr isotopic compositions are susceptible to late-stage effects, the homogeneous whole-rock Nd-Hf, zircon Hf, and apatite Nd isotopic compositions were used to trace the magma source, revealing that the parental magmas of the coarse-grained quartz monzonite, biotite monzogranite, and granite porphyry were derived from a common magma source.

The coarse-grained quartz monzonite, biotite monzogranite, and granite porphyry are characterized by moderately high SiO_2 contents (66.7–72.2 wt.%, 76.0–77.6 wt.%, 76.6–78.2 wt.%, respectively) and low MgO contents (0.04–0.43 wt.%, 0.03–0.26 wt.%, and 0.04–0.10 wt.%, respectively) (Figure 6 and Table S3), which are markedly distinct from the characteristic of the mantle (MgO > 3 wt.%). The coarse-grained quartz monzonite, biotite monzogranite, and granite porphyry have Nb/Ta values of 14.9–16.3, 9.5–12.8, and 11.2–12.9, respectively, with Zr/Hf values of 34.9–35.1, 20.9–27.7, and 20.3–28.7, respectively, which are similar to the Nb/Ta and Zr/Hf ratios (11.4 and 33, respectively) of the continental crust [80]. Furthermore, the $\delta^{18}O$ values of 5.7-6.7‰ of the coarse-grained quartz monzonite are higher than those of the mantle-derived dioritic enclave (4.5–6.2‰) in other coeval I-type granitic pluton (Shihuzhen-Jiudaogou pluton) near the study area [81], indicating that the coarse-grained quartz monzonite is characteristic of zircons crystallized from crust-derived magmas. Therefore, the different rock types in the Yushulinzi pluton may have been generated via the partial melting of crustal materials. The different rock types in the Yushulinzi pluton share enriched whole-rock Sr-Nd-Hf isotopic compositions and plot in the field defined by the ancient crust beneath the NCC on the $\varepsilon_{Nd}(t)$ vs. $(^{87}Sr/^{86}Sr)_i$ diagram (Figure 9). Their whole-rock Sr-Nd isotopic compositions are not only significantly distinct from the Early Cretaceous Guanshui pluton ($(^{87}Sr/^{86}Sr)_i$ = 0.70795, $\varepsilon_{Nd}(t)$ = −0.5) derived from the juvenile lower crust [26] but also the Early Cretaceous Qianshan pluton sourced from the upper crust beneath the Liaodong Peninsula [44]. In addition, the zircon grains extracted from the different rock types in the Yushulinzi pluton have $\varepsilon_{Hf}(t)$ values of −16.5 to −9.3 and corresponding Hf model ages (T_{2DM}) of 2456–3098 Ma (Figure 8 and Table S5). All of the rock samples from the Yushulinzi pluton plot in the field confined by the 1.8 Ga and 2.5 Ga crust evolutionary lines for the NCC (Figure 10), suggesting that the magma source of the Yushulinzi pluton potentially involved ancient crustal materials from the NCC. These ancient crustal materials have also been widely reported in studies conducted in the Liaodong Peninsula [47,82,83].

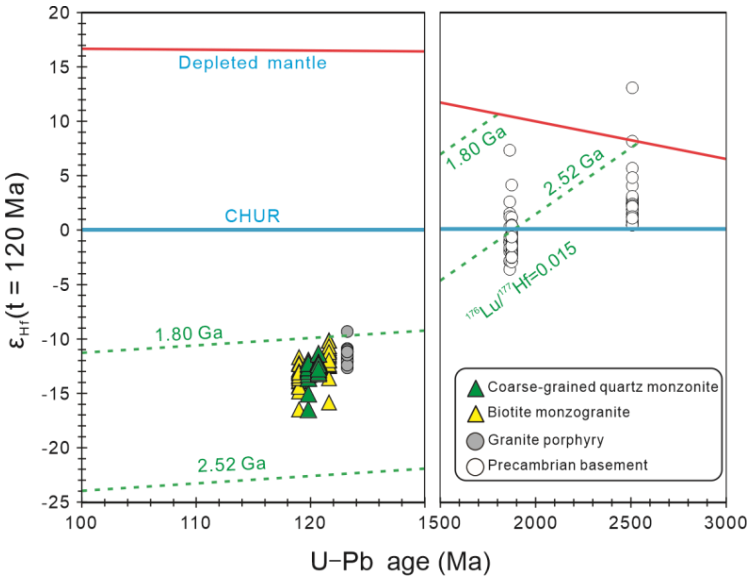


Figure 10. Plot of zircon $\varepsilon_{Hf}(t)$ value versus U-Pb age for the coarse-grained quartz monzonite, biotite monzogranite, and granite porphyry in the Yushulinzi pluton. All of the $\varepsilon_{Hf}(t)$ values were calculated from the zircon U-Pb ages. The data for the Precambrian basement are quoted from the literature [84–87].

Compared with the biotite monzogranite and granite porphyry, the coarse-grained quartz monzonite has relatively low SiO_2 (66.7–72.2 wt.%), CaO (0.1–0.2 wt.%), and K_2O (<0.2 wt.%) contents (Figure 6) and strong Rb, Ba, and K depletions (Figure 7b). However, rocks formed early in the fractional crystallization process have low SiO_2 and high CaO contents [88], which is notably different from the geochemical features of the coarse-grained quartz monzonite. Furthermore, extremely low Rb contents (<10 ppm, Table S3) cannot be generated solely via fractional crystallization, since Rb is highly incompatible [89]. Petrographic observations revealed the microstructures of the crystal accumulation in the coarse-grained quartz monzonite (Figure 2a). Consequently, the magma chamber of the Yushulinzi pluton may have undergone crystal-melt segregation processes, in which the coarse-grained quartz monzonite represents the crystal accumulation formed in the early stage, and the segregated melts formed biotite monzogranite and granite porphyry following magma evolution. Notably, the coarse-grained quartz monzonite is characterized by low CaO, K_2O, and Rb contents and high Na_2O contents, suggesting crystal accumulation dominated by albite, with low contents of K-feldspar.

During the Early Cretaceous, intense magmatism, large-scale tectonic activities and mineralization occurred across the NCC, representing the shallow crustal response to the NCC destruction [29,37,39,90–93]. The coarse-grained quartz monzonite, biotite monzogranite, and granite porphyry in the Yushulinzi pluton were formed between 123 Ma and 119 Ma and were coeval with the development of metamorphic core complexes and pull-apart basins [55,94–97], suggesting that they were formed in an extensional environment related to the NCC destruction. In summary, the Yushulinzi pluton was formed during the NCC destruction, and the partial melting of ancient crustal materials generated the parental magmas that formed the coarse-grained monzonite, biotite monzogranite, and granite porphyry through crystal-melt segregation processes.

5.2. Tracing Magmatic Evolution Using Apatite Sr and Zircon Hf Isotopic Compositions

The variations in the composition, temperature, and pressure of the primitive magma resulting from different magmatic processes were documented well by the growth of the minerals (in particular the early crystallization of accessory minerals) [98]. Thus, in situ element and isotopic analyses of accessory minerals can provide a more effective tracer of magma sources and evolutionary processes compared to whole-rock geochemistry. As previously mentioned, the Nd-Hf isotopic compositions of the whole-rock and accessory minerals (apatite and zircon) indicate that the different rock types in the Yushulinzi pluton were derived from a common magma source. However, the coarse-grained quartz monzonite and biotite monzogranite exhibit a wide range of apatite Sr isotopic compositions (Figure 9). In addition, slight differences in the peak $\varepsilon_{Hf}(t)$ values can be seen in Figure 8, although the coarse-grained quartz monzonite, biotite monzogranite, and granite porphyry have similar $\varepsilon_{Hf}(t)$ ranges. In summary, the Yushulinzi pluton probably experienced diverse magmatism during the evolutionary processes.

The coarse-grained quartz monzonite, biotite monzogranite, and granite porphyry in the Yushulinzi pluton are characterized by heterogeneous whole-rock Sr isotopic compositions. The coarse-grained quartz monzonite has significantly high whole-rock $(^{87}Sr/^{86}Sr)_i$ ratios (0.71413 to 0.71951), while the biotite monzogranite has relatively low whole-rock $(^{87}Sr/^{86}Sr)_i$ ratios (0.70462 to 0.70824) (Table S4). However, it is difficult to determine the origins of these variations via the whole-rock geochemistry. The apatite Sr isotopic compositions of the coarse-grained quartz monzonite and biotite monzogranite are not significantly different (Figure 9 and Table S6). This conclusion is remarkably distinct from those based on the whole-rock Sr isotopic compositions of their host rocks. Moreover, the apatite grain from the coarse-grained quartz monzonite and biotite monzogranite have $(^{87}Sr/^{86}Sr)_i$ ratio ranges of 0.70960–0.71577 and 0.70945–0.71321, respectively, which are unlikely to be caused by the analytical errors (Figure 9 and Table S6). The apatite Sr isotopic compositions of the coarse-grained quartz monzonite and biotite monzogranite exhibit a change trend toward high $(^{87}Sr/^{86}Sr)_i$ values on the $\varepsilon_{Nd}(t)$ vs. $(^{87}Sr/^{86}Sr)_i$ plot (Figure 9),

with some samples plotting within the field of the Early Cretaceous Qianshan A-type granite pluton derived from the felsic upper crust [44]. Based on previous studies [44], the origin of the Yushulinzi pluton may involve the addition of crustal materials with high $(^{87}Sr/^{86}Sr)_i$ values, such as shallow crustal materials. Additionally, the whole-rock $(^{87}Sr/^{86}Sr)_i$ value of sample 08JF76 (coarse-grained quartz monzonite) is greater than its corresponding apatite $(^{87}Sr/^{86}Sr)_i$ value (Figure 9 and Table S6), which provides further evidence of the incorporation of shallow crustal materials.

The peak zircon $\varepsilon_{Hf}(t)$ values of the granite porphyry are slightly higher than that of the coarse-grained quartz monzonite (Figure 8a). Furthermore, the biotite monzogranite has a broader range of $\varepsilon_{Hf}(t)$ values (−16.5 to −10.2) than the coarse-grained quartz monzonite (−16.5 to −11.4) and granite porphyries (−12.7 to −9.3) and exhibits a bimodal distribution (Figure 8b). This suggests that the residual melts remaining after the crystal-melt segregation processes may have experienced the incorporation of external materials with relatively high $\varepsilon_{Hf}(t)$ values, resulting in the evolution of the biotite monzogranite and granite porphyry toward low negative $\varepsilon_{Hf}(t)$ values. In contrast, the different rock types in the Yushulinzi pluton are characterized by homogeneous whole-rock Hf isotopic compositions, which fail to document the above variation.

Taken together, the Yushulinzi pluton was predominately derived from the partial melting of the ancient crustal materials beneath the NCC, followed by the crystal-melt segregation process, which generated the coarse-grained quartz monzonite, biotite monzogranite, and granite porphyry. In addition, the in situ apatite Sr and zircon Hf isotopic compositions indicate the incorporation of shallow crustal components and materials with high zircon $\varepsilon_{Hf}(t)$ values during the magma evolution. Consequently, the in situ apatite Sr and zircon Hf isotopes can provide critical information on magma evolution.

6. Conclusions

The coarse-grained quartz monzonite, biotite monzogranite, and granite porphyry in the Yushulinzi pluton, Liaodong Peninsula, eastern NCC, have identical zircon U-Pb ages of 123–119 Ma and represent the magmatism that took place during the NCC destruction. We integrated whole-rock geochemistry and in situ apatite Sr-Nd and in situ zircon Hf-O isotopic analyses of the different rock types in the Yushulinzi pluton to determine that the coarse-grained quartz monzonite, biotite monzogranite, and granite porphyry were mainly derived from the partial melting of the ancient crustal materials beneath the NCC, and the petrogenetic processes included crystal-melt segregation processes. The variable apatite Sr and zircon Hf isotopic compositions reveal the addition of shallow crust components and materials with high $\varepsilon_{Hf}(t)$ values during the magma evolution, which are not revealed by the whole-rock geochemistry. The results of this study highlight that the integration of in situ apatite Sr-Nd and zircon Hf-O isotopic compositions provides an excellent method for tracing the magma source and petrogenetic processes of the granitic system, which are critical for elucidating the petrogenesis of granitoids.

Supplementary Materials: The following information can be downloaded at: https://www.mdpi.com/article/10.3390/min13040545/s1, Table S1: Zircon LA-ICP-MS U-Pb dating results for the coarse-grained quartz monzonite, biotite monzogranite, and granite porphyry in the Yushulinzi pluton; Table S2: Zircon SIMS U-Pb dating results for the coarse-grained quartz monzonite in the Yushulinzi pluton; Table S3: Major element oxide (wt.%) and trace element concentrations (ppm) of the studied samples from the Yushulinzi pluton; Table S4: Wholerock Sr-Nd-Hf isotopic compositions of the studied samples from the Yushulinzi pluton; Table S5: In situ zircon Hf-O isotopic compositions of the studied samples from the Yushulinzi pluton; Table S6: In situ apatite Sr-Nd isotopic compositions of the studied samples from the Yushulinzi pluton.

Author Contributions: Conceptualization, M.L. and J.S.; methodology, J.S.; software, M.L.; validation, M.L., Z.L., J.S. and J.Z.; formal analysis, M.L.; investigation, M.L., Z.L., J.S. and J.Z.; resources, J.S.; data curation, Z.L.; writing—original draft preparation, M.L.; writing—review and editing, M.L. and J.S.; visualization, M.L.; supervision, J.S. and J.Z.; project administration, J.S.; funding acquisition, J.S. All authors have read and agreed to the published version of the manuscript.

Funding: This research was funded by the National Natural Science Foundation of China (No. 42073034) and the Fundamental Research Funds for the Central Universities (E0E48915X2).

Data Availability Statement: Datasets for this study are presented in this paper.

Acknowledgments: The authors thank Qiu-Li Li and Lie-Wen Xie for their help with zircon U-Pb dating and in situ isotopic analyses and Chao-Feng Li for help with whole-rock Sr-Nd-Hf isotopic analyses, respectively. We are grateful for constructive comments and suggestions from the Editor and anonymous reviewers.

Conflicts of Interest: The authors declare no conflict of interest.

References

1. Kemp, A.I.S.; Hawkesworth, C.J.; Foster, G.L.; Paterson, B.A.; Woodhead, J.D.; Hergt, J.M.; Gray, C.M.; Whitehouse, M.J. Magmatic and crustal differentiation history of granitic rocks from Hf-O isotopes in zircon. *Science* **2007**, *315*, 980–983. [CrossRef] [PubMed]
2. Chappell, B.W.; Stephens, W.E. Origin of infracrustal (I-type) granite magmas. *Trans. R. Soc. Edinb. Earth Sci.* **1988**, *79*, 71–86. [CrossRef]
3. Guo, F.; Huang, M.; Zhao, L. Nd-Hf-O isotopic evidence for subduction-induced crustal replacement in NE China. *Chem. Geol.* **2019**, *525*, 125–142. [CrossRef]
4. Han, B.F. Diverse post-collisional granitoids and their tectonic setting discrimination. *Earth Sci. Front.* **2007**, *14*, 64–72. (In Chinese with English abstract)
5. Wang, T.; Guo, L.; Li, S.; Wang, X.X.; Wang, Z.Y. Some important issues in the study of granite tectonics. *J. Geom.* **2019**, *25*, 899–919. (In Chinese with English abstract)
6. Zhu, D.C.; Wang, Q.; Zhao, Z.D.; Niu, Y.L.; Hou, Z.Q.; Pan, G.T.; Mo, X.X. Magmatic origin of continental arcs and continental crust formation. *Earth Sci. Front.* **2018**, *25*, 67–77. (In Chinese with English abstract)
7. Wang, T.; Guo, L.; Zheng, Y.D.; Donskaya, T.; Gladkochub, D.; Zeng, L.S.; Li, J.B.; Wang, Y.B.; Mazukabzov, A. Timing and processes of late Mesozoic mid-lower-crustal extension in continental NE Asia and implications for the tectonic setting of the destruction of the North China Craton: Mainly constrained by zircon U-Pb ages from metamorphic core complexes. *Lithos* **2012**, *154*, 315–345. [CrossRef]
8. Yang, J.H.; Wu, F.Y.; Chung, S.L.; Wilde, S.A.; Chu, M.F. Multiple sources for the origin of granites: Geochemical and Nd/Sr isotopic evidence from the Gudaoling granite and its mafic enclaves, northeast China. *Geochim. Cosmochim. Acta* **2004**, *68*, 4469–4483. [CrossRef]
9. Depaolo, D.J. Trace element and isotopic effects of combined wallrock assimilation and fractional crystallization. *Earth Planet. Sci. Lett.* **1981**, *53*, 189–202. [CrossRef]
10. Ma, C.Q.; Li, Y.Q. Incremental growth of granitoid plutons and highly crystalline magmatic differentiation. *Acta Petro. Sin.* **2017**, *33*, 1479–1488. (In Chinese with English abstract)
11. Jiang, D.S.; Xu, X.S.; Xia, Y.; Erdmann, S. Magma Mixing in a Granite and Related Rock Association: Insight from Its Mineralogical, Petrochemical and "Reversed Isotope" Features. *J. Geophys. Res. Solid Earth.* **2018**, *123*, 2262–2285. [CrossRef]
12. Griffin, W.L.; Wang, X.; Jackson, S.E.; Pearson, N.J.; O'Reilly, S.Y.; Xu, X.S.; Zhou, X.M. Zircon chemistry and magma mixing, SE China: In-situ analysis of Hf isotopes, Tonglu and Pingtan igneous complexes. *Lithos* **2002**, *61*, 237–269. [CrossRef]
13. Yang, J.H.; Wu, F.Y.; Wilde, S.A.; Xie, L.W.; Yang, Y.H.; Liu, X.M. Tracing magma mixing in granite genesis: In situ U-Pb dating and Hf-isotope analysis of zircons. *Contrib. Mineral. Petrol.* **2007**, *153*, 177–190. [CrossRef]
14. Griffin, W.L.; Pearson, N.J.; Belousova, E.; Jackson, S.E.; Achterbergh, E.; O'Reilly, S.Y.; Shee, S.R. The Hf isotope composition of cratonic mantle: LAM-MC-ICPMS analysis of zircon megacrysts in kimberlites. *Geochim. Cosmochim. Acta* **2000**, *64*, 133–147. [CrossRef]
15. Xu, X.; He, Z. Progress in Granite Studies. *Bull. Mineral. Petrol. Geochem.* **2012**, *31*, 205–209. (In Chinese with English abstract)
16. Wu, Y.B.; Zheng, Y.F. Genesis of zircon and its constraints on interpretation of U-Pb age. *Chin. Sci. Bull.* **2004**, *49*, 1554–1569. (In Chinese with English abstract) [CrossRef]
17. Yuan, H.L.; Gao, S.; Dai, M.N.; Zong, C.L.; Günther, D.; Fontaine, G.H.; Liu, X.M.; Diwu, C. Simultaneous determinations of U-Pb age, Hf isotopes and trace element compositions of zircon by excimer laser-ablation quadrupole and multiple-collector ICP-MS. *Chem. Geol.* **2008**, *247*, 100–118. [CrossRef]
18. Zhao, Z.F.; Zheng, Y.F.; Chen, Y.X.; Sun, G.C. Partial melting of subducted continental crust: Geochemical evidence from synexhumation granite in the Sulu orogen. *Geol. Soc. Am. Bull.* **2017**, *129*, 1692–1707. [CrossRef]
19. Decrée, S.; Cawthorn, G.; Deloule, E.; Mercadier, J.; Frimmel, H.; Baele, J.M. Unravelling the processes controlling apatite formation in the Phalaborwa Complex (South Africa) based on combined cathodoluminescence, LA-ICPMS and in-situ O and Sr isotope analyses. *Contrib. Mineral. Petro.* **2020**, *175*, 1–31. [CrossRef]
20. Laurent, O.; Zeh, A.; Gerdes, A.; Villaros, A.; Gros, K.; Słaby, E. How do granitoid magmas mix with each other? Insights from textures, trace element and Sr-Nd isotopic composition of apatite and titanite from the Matok pluton (South Africa). *Contrib. Mineral. Petro.* **2017**, *172*, 9–80. [CrossRef]

21. Sun, J.F.; Yang, J.H.; Wu, F.Y.; Li, X.H.; Yang, Y.H.; Xie, L.W.; Wilde, S.A. Magma mixing controlling the origin of the Early Cretaceous Fangshan granitic pluton, North China Craton In situ U-Pb age and Sr-, Nd-, Hf- and O-isotope evidence. *Lithos* **2010**, *120*, 421–438. [CrossRef]
22. Sun, J.F.; Yang, J.H.; Zhang, J.H.; Yang, Y.H.; Zhu, Y.S. Apatite geochemical and SrNd isotopic insights into granitoid petrogenesis. *Chem. Geol.* **2021**, *566*, 120104. [CrossRef]
23. Cao, M.J.; Qin, K.Z.; Evans, N.J.; Li, G.M.; Ling, X.; McInnes, B.I.A.; Zhao, J.X. Titanite in situ SIMS U–Pb geochronology, elemental and Nd isotopic signatures record mineralization and fluid characteristics at the Pusangguo skarn deposit, Tibet. *Miner. Depos.* **2021**, *56*, 907–916. [CrossRef]
24. Sun, J.F.; Zhang, J.H.; Yang, J.H.; Yang, Y.H.; Chen, S. Tracing magma mixing and crystal-melt segregation in the genesis of syenite with mafic enclaves: Evidence from in situ zircon Hf-O and apatite Sr-Nd isotopes. *Lithos* **2019**, *334*, 42–57. [CrossRef]
25. Wu, F.Y.; Xu, Y.G.; Gao, S.; Zheng, J.P. Controversial on studies of the lithospheric thinning and craton destruction of North China. *Acta Petrol. Sin.* **2008**, *24*, 1145–1174. (In Chinese with English abstract)
26. Yang, J.H.; Wu, F.Y.; Wilde, S.A.; Belousova, E.; Griffin, W.L. Mesozoic decratonization of the North China block. *Geology* **2008**, *36*, 467–470. [CrossRef]
27. Zhu, R.X.; Chen, L.; Wu, F.Y.; Liu, J.L. Timing, scale and mechanism of the destruction of the North China Craton. *Sci. China Earth Sci.* **2011**, *54*, 789–797. [CrossRef]
28. Wu, F.Y.; Xu, Y.G.; Zhu, R.X.; Zhang, G.W. Thinning and destruction of the cratonic lithosphere: A global perspective. *Sci. China Earth Sci.* **2014**, *57*, 2878–2890. [CrossRef]
29. Wu, F.Y.; Lin, J.Q.; Wilde, S.A.; Zhang, X.O.; Yang, J.H. Nature and significance of the Early Cretaceous giant igneous event in eastern China. *Earth Planet. Sci. Lett.* **2005**, *233*, 103–119. [CrossRef]
30. Wu, F.Y.; Yang, J.H.; Wilde, S.A.; Zhang, X.O. Geochronology, petrogenesis and tectonic implications of Jurassic granites in the Liaodong Peninsula, NE China. *Chem. Geol.* **2005**, *221*, 127–156. [CrossRef]
31. Meng, Q.R. What drove late Mesozoic extension of the northern China-Mongolia tract? *Tectonophysics* **2003**, *369*, 155–174. [CrossRef]
32. Yang, J.H.; Wu, F.Y.; Chung, S.L.; Lo, C.H.; Wilde, S.A.; Davis, G.A. Rapid exhumation and cooling of the Liaonan metamorphic core complex: Inferences from 40Ar/39Ar thermochronology and implications for Late Mesozoic extension in the eastern North China Craton. *Geol. Soc. Am. Bull.* **2007**, *119*, 1405–1414. [CrossRef]
33. Zhu, G.; Jiang, D.Z.; Zhang, B.L.; Chen, Y. Destruction of the eastern North China Craton in a backarc setting: Evidence from crustal deformation kinematics. *Gondwana Res.* **2012**, *22*, 86–103. [CrossRef]
34. Lin, W.; Zeng, J.P.; Meng, L.T.; Qiu, H.B.A.; Wei, W.; Ren, Z.H.; Chu, Y.; Li, S.J.; Song, C.; Wang, Q.C. Extensional tectonics and North China Craton destruction: Insights from the magnetic susceptibility anisotropy (AMS) of granite and metamorphic core complex. *Sci. China Earth Sci.* **2021**, *64*, 1557–1589. [CrossRef]
35. Mao, J.W.; Wang, Y.T.; Zhang, Z.H.; Yu, J.J.; Niu, B.G. Geodynamic settings of Mesozoic large-scale mineralization in North China and adjacent areas—Implication from the highly precise and accurate ages of metal deposits. *Sci. China Ser. D Earth Sci.* **2003**, *46*, 838–851. [CrossRef]
36. Zhu, R.X.; Fan, H.R.; Li, J.W.; Meng, Q.R.; Li, S.R.; Zeng, Q.D. Decratonic gold deposits. *Sci. China Earth Sci.* **2015**, *58*, 1523–1537. [CrossRef]
37. Zhu, R.X.; Zhang, H.F.; Zhu, G.; Meng, Q.R.; Fan, H.R.; Yang, J.H.; Wu, F.Y.; Zhang, Z.Y.; Zheng, T.Y. Craton destruction and related resources. *Int. J. Earth Sci.* **2017**, *106*, 2233–2257. [CrossRef]
38. Zeng, Q.D.; Wang, Y.B.; Yang, J.H.; Guo, Y.P.; Yu, B.; Zhou, L.L.; Qiu, H.C. Spatial-temporal distribution and tectonic setting of gold deposits in the Northern margin gold belt of the North China Craton. *Int. Geol. Rev.* **2021**, *63*, 941–972. [CrossRef]
39. Li, J.W.; Bi, S.J.; Selby, D.; Chen, L.; Vasconcelos, P.; Thiede, D.; Zhou, M.F.; Zhao, X.F.; Li, Z.K.; Qiu, H.N. Giant Mesozoic gold provinces related to the destruction of the North China craton. *Earth Planet. Sci. Lett.* **2012**, *349*, 26–37. [CrossRef]
40. Zhu, R.X.; Xu, Y.G.; Zhu, G.; Zhang, H.F.; Xia, Q.K.; Zheng, T.Y. Destruction of the North China Craton. *Sci. China Earth Sci.* **2012**, *55*, 1565–1587. [CrossRef]
41. Pei, F.P.; Xu, W.L.; Yu, Y.; Zhao, Q.G.; Yang, D.B. Petrogenesis of the Late Triassic Mayihe Pluton in Southern Jilin Province: Evidence from Zircon U-Pb Geochronology and Geochemistry. *J. Jilin Univ.* **2008**, *3*, 351–362. (In Chinese with English abstract)
42. Wu, F.Y.; Yang, J.H.; Liu, X.M. Geochronological Framework of the Mesozoic Granitic Magmatism in the Liaodong Peninsula Northeast China. *Geol. J. China Univ.* **2005**, *11*, 305–317. (In Chinese with English abstract)
43. Sun, J.F.; Yang, J.H. Mesozoic magmatism related to decratonization of the North China Craton. *Acta Petrol. Mineral.* **2013**, *32*, 577–592. (In Chinese with English abstract)
44. Yang, J.H.; Wu, F.Y.; Chung, S.L.; Wilde, S.A.; Chu, M.F. A hybrid origin for the Qianshan A-type granite, northeast China: Geochemical and Sr-Nd-Hf isotopic evidence. *Lithos* **2006**, *89*, 89–106. [CrossRef]
45. Yang, J.H.; Sun, J.F.; Chen, F.; Wilde, S.A.; Wu, F.Y. Sources and petrogenesis of late triassic dolerite dikes in the liaodong peninsula: Implications for post-collisional lithosphere thinning of the eastern North China Craton. *J. Petrol.* **2007**, *48*, 1973–1997. [CrossRef]
46. Liu, D.Y.; Nutman, A.P. Compston W, Wu JS, Shen QH: Remnants of ≥3800 Ma crust in the Chinese part of the Sino-Korean craton. *Geology* **1992**, *20*, 339–342. [CrossRef]
47. Wu, F.Y.; Zhang, Y.B.; Yang, J.H.; Xie, L.W.; Yang, Y.H. Zircon U-Pb and Hf isotopic constraints on the Early Archean crustal evolution in Anshan of the North China Craton. *Precambrian Res.* **2008**, *167*, 339–362. [CrossRef]

48. Luo, Y.; Sun, M.; Zhao, G.C.; Li, S.Z.; Xu, P.; Ye, K.; Xia, X.P. LA-ICP-MS U-Pb zircon ages of the Liaohe Group in the Eastern Block of the North China Craton: Constraints on the evolution of the Jiao-Liao-Ji Belt. *Precambrian Res.* **2004**, *134*, 349–371. [CrossRef]
49. Xie, L.W.; Yang, J.H.; Wu, F.Y.; Yang, Y.H.; Wilde, S.A. PbSL dating of garnet and staurolite: Constraints on the Paleoproterozoic crustal evolution of the Eastern Block, North China Craton. *J. Asian Earth Sci.* **2011**, *42*, 142–154. [CrossRef]
50. Dong, Y.; Bi, J.H.; Xing, D.H.; Ge, W.C.; Yang, H.; Hao, Y.J.; Ji, Z.; Jing, Y. Geochronology and geochemistry of Liaohe Group and Liaoji granitoid in the Jiao-Liao-Ji Belt, North China Craton: Implications for petrogenesis and tectonic evolution. *Precambrian Res.* **2019**, *332*, 105399. [CrossRef]
51. Wang, H.Z.; Mo, X.X. An outline of the tectonic evolution of China. *Episodes* **1995**, *18*, 6–16. [CrossRef] [PubMed]
52. Zhu, Y.S.; Yang, J.H.; Sun, J.F.; Zhang, J.H.; Wu, F.Y. Petrogenesis of coeval silica-saturated and silica-undersaturated alkaline rocks: Mineralogical and geochemical evidence from the Saima alkaline complex, NE China. *J. Asian Earth Sci.* **2016**, *117*, 184–207. [CrossRef]
53. Yang, J.H.; Sun, J.F.; Zhang, J.H.; Wilde, S.A. Petrogenesis of Late Triassic intrusive rocks in the northern Liaodong Peninsula related to decratonization of the North China Craton: Zircon U-Pb age and Hf-O isotope evidence. *Lithos* **2012**, *153*, 108–128. [CrossRef]
54. Yang, J.H.; Wu, F.Y.; Wilde, S.A.; Liu, X.M. Petrogenesis of Late Triassic granitoids and their enclaves with implications for post-collisional lithospheric thinning of the Liaodong Peninsula, North China Craton. *Chem. Geol.* **2007**, *242*, 155–175. [CrossRef]
55. Pei, F.P.; Xu, W.L.; Yang, D.B.; Yu, Y.; Meng, E.; Zhao, Q.G. Petrogenesis of late Mesozoic granitoids in southern Jilin province, northeastern China: Geochronological, geochemical, and Sr-Nd-Pb isotopic evidence. *Lithos* **2011**, *125*, 27–39. [CrossRef]
56. Yang, Y.H.; Zhang, H.F.; Chu, Z.Y.; Xie, L.W.; Wu, F.Y. Combined chemical separation of Lu, Hf, Rb, Sr, Sm and Nd from a single rock digest and precise and accurate isotope determinations of Lu-Hf, Rb-Sr and Sm-Nd isotope systems using Multi-collector ICP-MS and TIMS. *Int. J. Mass Spectrom.* **2010**, *290*, 120–126. [CrossRef]
57. Yang, Y.H.; Chu, Z.Y.; Wu, F.Y.; Xie, L.W.; Yang, J.H. Precise and accurate determination of Sm, Nd concentrations and Nd isotopic compositions in geological samples by MC-ICP-MS. *J. Anal. At. Spectrom.* **2011**, *26*, 1237–1244. [CrossRef]
58. Weis, D.; Kieffer, B.; Maerschalk, C.; Pretorius, W.; Barling, J. High-precision Pb-Sr-Nd-Hf isotopic characterization of USGS BHVO-1 and BHVO-2 reference materials. *Geochem. Geophys. Geosyst.* **2005**, *6*. [CrossRef]
59. Weis, D.; Kieffer, B.; Maerschalk, C.; Barling, J.; Jong, J.D.; Williams, G.A.; Hanano, D.; Pretorius, W.; Mattielli, N.; Scoates, J.S.; et al. High-precision isotopic characterization of USGS reference materials by TIMS and MC-ICP-MS. *Geochem. Geophys. Geosyst.* **2006**, *7*, Q08006. [CrossRef]
60. Weis, D.; Kieffer, B.; Hanano, D.; Nobre Silva, I.; Barling, J.; Pretorius, W.; Maerschalk, C.; Mattielli, N. Hf isotope compositions of U.S. Geological Survey reference materials. *Geochem. Geophys. Geosyst.* **2007**, *8*, Q06006. [CrossRef]
61. Li, X.H.; Li, W.X.; Wang, X.C.; Li, Q.L.; Liu, Y.; Tang, G.Q. Role of mantle-derived magma in genesis of early Yanshanian granites in the Nanling Range, South China: In situ zircon Hf-O isotopic constraints. *Sci. China Ser. D Earth Sci.* **2009**, *52*, 1262–1278. [CrossRef]
62. Li, X.H.; Long, W.G.; Li, Q.L.; Liu, Y.; Zheng, Y.F.; Yang, Y.H.; Chamberlain, K.R.; Wan, D.F.; Guo, C.H.; Wang, X.C.; et al. Penglai Zircon Megacrysts: A Potential New Working Reference Material for Microbeam Determination of Hf-O Isotopes and U-Pb Age. *Geostand. Geoanal. Res.* **2010**, *34*, 117–134. [CrossRef]
63. Black, L.P.; Kamo, S.L.; Allen, C.M.; Davis, D.W.; Aleinikoff, J.N.; Valley, J.W.; Mundil, R.; Campbell, I.H.; Korsch, R.J.; Williams, I.S.; et al. Improved 206Pb/238U microprobe geochronology by the monitoring of a trace-element-related matrix effect; SHRIMP, ID-TIMS, ELA-ICP-MS and oxygen isotope documentation for a series of zircon standards. *Chem. Geol.* **2004**, *205*, 115–140. [CrossRef]
64. Ludwig, K.R. *User's Manual for IsoPlot 3.0: A Geochronological Toolkit for Microsoft Excel*; Berkeley Geochronology Center Special Publications: Berkeley, CA, USA, 2003.
65. Li, X.H.; Tang, G.Q.; Gong, B.; Yang, Y.H.; Hou, K.J.; Hu, Z.C.; Li, Q.L.; Liu, Y.; Li, W.X. Qinghu zircon: A working refrence for microbeam analysis of U-Pb age and Hf and O isotopes. *Chin. Sci. Bull.* **2013**, *58*, 4647–4654. [CrossRef]
66. Xie, L.W.; Zhang, Y.B.; Zhang, H.H.; Sun, J.F.; Wu, F.Y. In situ simultaneous determination of trace elements, U-Pb and Lu-Hf isotopes in zircon and baddeleyite. *Chin. Sci. Bull.* **2008**, *53*, 1565–1573. [CrossRef]
67. Wu, F.Y.; Yang, Y.H.; Xie, L.W.; Yang, J.H.; Xu, P. Hf isotopic compositions of the standard zircons and baddeleyites used in U-Pb geochronology. *Chem. Geol.* **2006**, *234*, 105–126. [CrossRef]
68. Andersen, T. Correction of common lead in U-Pb analyses that do not report 204Pb. *Chem. Geol.* **2002**, *192*, 59–79. [CrossRef]
69. Griffin, W.L.; Powell, W.I.; Pearson, N.J.; O' Reilly, S.Y. GLITTER: Data Reduction Software for Laser Ablation ICP–MS. Laser Ablation-ICP-MS in the Earth Sciences. *Mineral. Assoc. Can. Short Course Ser.* **2008**, *40*, 204–207.
70. Zeh, A.; Gerdes, A.; Klemd, R.; Barton, J.M. Archaean to Proterozoic Crustal Evolution in the Central Zone of the Limpopo Belt (South Africa-Botswana): Constraints from Combined U-Pb and Lu-Hf Isotope Analyses of Zircon. *J. Petrol.* **2007**, *48*, 1605–1639. [CrossRef]
71. Goolaerts, A.; Mattielli, N.; Jong, J.; Weis, D.; Scoates, J.S. Hf and Lu isotopic reference values for the zircon standard 91500 by MC-ICP-MS. *Chem. Geol.* **2004**, *206*, 1–9. [CrossRef]
72. Yang, Y.H.; Wu, F.Y.; Yang, J.H.; Chew, D.M.; Xie, L.W.; Chu, Z.Y.; Zhang, Y.B.; Huang, C. Sr and Nd isotopic compositions of apatite reference materials used in U-Th-Pb geochronology. *Chem. Geol.* **2014**, *385*, 35–55. [CrossRef]

73. Yang, Y.H.; Wu, F.Y.; Wilde, S.A.; Liu, X.M.; Zhang, Y.B.; Xie, L.W.; Yang, J.H. In situ perovskite Sr-Nd isotopic constraints on the petrogenesis of the Ordovician Mengyin kimberlites in the North China Craton. *Chem. Geol.* **2009**, *264*, 24–42. [CrossRef]
74. Yang, Y.H.; Sun, J.F.; Xie, L.W.; Fan, H.R.; Wu, F.Y. In situ Nd isotopic measurement of natural geological materials by LA-MC-ICPMS. *Chin. Sci. Bull.* **2008**, *53*, 1062–1070. [CrossRef]
75. McFarlane, C.R.M.; McCulloch, M.T. Coupling of in-situ Sm-Nd systematics and U-Pb dating of monazite and allanite with applications to crustal evolution studies. *Chem. Geol.* **2007**, *245*, 45–60. [CrossRef]
76. Sun, S.S.; McDonough, W.F. Chemical and isotopic systematics of oceanic basalts: Implications for mantle composition and processes. *Geol. Soc. Lond. Spec. Publ.* **1989**, *42*, 313–345. [CrossRef]
77. Jahn, B.M.; Wu, F.Y.; Lo, C.H.; Tsai, C.H. Crust-mantle interaction induced by deep subduction of the continental crust: Geochemiand Sr-Nd isotopic evidence from post-collisional mafic-ultramafic intrusions of the northern Dabie complex, central China. *Chem. Geol.* **1999**, *157*, 119–146. [CrossRef]
78. Wu, F.Y.; Ge, W.C.; Sun, D.Y.; Lin, Q.; Zhou, Y. The Sm-Nd, Rb-Sr isotopic ages of the Archean Granites in southern Jilin province. *Acta Petrol. Sin.* **1997**, *4*, 50–57. (In Chinese with English abstract)
79. Pei, F.P.; Xu, W.L.; Yang, D.B.; Yu, Y.; Meng, E. Heterogeneity of Late Mesozoic deep lithosphere beneath the northeastern North China Craton: Evidence from elemental and Sr–Nd isotopic geochemistry of Mesozoic volcanic rocks in southern Jilin province, China. *Acta Petrol. Sin.* **2009**, *25*, 1962–1972. (In Chinese with English abstract)
80. Weaver, B.L.; Tarney, J. Empirical approach to estimating the composition of the continental crust. *Nature* **1984**, *310*, 575–577. [CrossRef]
81. Chen, S.; Sun, J.F.; Zhang, J.H.; Yang, J.H.; Yang, Y.H. Genetic links between granitic and related dioritic rocks in Liaodong Peninsula, China: Sr-Nd-Hf-O isotopic evidence. *Lithos* **2020**, *356–357*, 105368. [CrossRef]
82. Lu, X.P.; Wu, F.Y.; Lin, J.Q.; Sun, D.Y.; Zhang, Y.B.; Guo, L.C. Geochronological successions of the early Precambrian granitic magmatism in southern Liaodong peninsula and its constraints on tectonic evolution of the North China Craton. *Chin. J. Geol.* **2004**, *39*, 123–138. (In Chinese with English abstract)
83. Lu, X.P.; Wu, F.Y.; Guo, J.H.; Wilde, S.A.; Yang, J.H.; Liu, X.M.; Zhang, X.O. Zircon U-Pb geochronological constraints on the Paleoproterozoic crustal evolution of the Eastern block in the North China Craton. *Precambrian Resh.* **2006**, *146*, 138–164. [CrossRef]
84. Wu, F.Y.; Yang, J.H.; Liu, X.M.; Li, T.S.; Xie, L.W.; Yang, Y.H. Hf isotopes of the 3.8 Ga zircons in eastern Hebei Province, China: Implications for early crustal evolution of the North China Craton. *Chin. Sci. Bull.* **2005**, *50*, 2473–2480. [CrossRef]
85. Yang, J.H.; Wu, F.Y.; Liu, X.M.; Xie, L.W. Zircon U-Pb ages and Hf isotopes and their geological significance of the Miyun rapakivi granites from Beijing, China. *Acta Petrol. Sin.* **2005**, *21*, 1633–1644, (In Chinese with English abstract).
86. Yang, J.H.; Wu, F.Y.; Wilde, S.A.; Zhao, G.C. Petrogenesis and geodynamics of Late Archean magmatism in eastern Hebei, eastern North China Craton: Geochronological, geochemical and Nd-Hf isotopic evidence. *Precambrian Res.* **2008**, *167*, 125–149. [CrossRef]
87. Zhang, S.H.; Liu, S.W.; Zhao, Y.; Yang, J.H.; Song, B.; Liu, X.M. The 1.75–1.68Ga anorthosite-mangerite-alkali granitoid-rapakivi granite suite from the northern North China Craton: Magmatism related to a Paleoproterozoic orogen. *Precambrian Res.* **2007**, *155*, 287–312. [CrossRef]
88. Wang, L.X.; Ma, C.Q.; Zhang, C.; Zhang, J.Y.; Marks, M.A.W. Genesis of leucogranite by prolonged fractional crystallization: A case study of the Mufushan complex, South China. *Lithos* **2014**, *206*, 147–163. [CrossRef]
89. Halliday, A.N.; Davidson, J.P.; Hildreth, W.; Holden, P. Modeling the petrogenesis of high Rb/Sr silicic magmas. *Chem. Geol.* **1991**, *92*, 107–114. [CrossRef]
90. Zeng, J.P.; Lin, W.; Qiu, H.B.; Wei, W.; Meng, L.T.; Chu, Y.; Ren, Z.H.; Wang, Y.; Feng, Z.T. When did the large-scale extensional tectonics begin in North China Craton? *Tectonophysics* **2022**, *840*, 229563. [CrossRef]
91. Meng, Q.R.; Hu, J.M.; Jin, J.Q.; Zhang, Y.; Xu, D.F. Tectonics of the late Mesozoic wide extensional basin systemin the China-Mongolia border region. *Basin Res.* **2003**, *15*, 397–415. [CrossRef]
92. Lin, W.; Faure, M.; Chen, Y.; Ji, W.B.; Wang, F.; Wu, L.L.; Charles, N.; Wang, J.; Wang, Q.C. Late Mesozoic compressional to extensional tectonics in the Yiwulüshan massif, NE China and its bearing on the evolution of the Yinshan-Yanshan orogenic belt. Part I: Structural analyses and geochronological constraints. *Gondwana Res.* **2013**, *23*, 54–77. [CrossRef]
93. Zhu, G.; Chen, Y.; Jiang, D.Z.; Lin, S.Z. Rapid change from compression to extension in the North China Craton during the Early Cretaceous: Evidence from the Yunmengshan metamorphic core complex. *Tectonophysics* **2015**, *656*, 91–110. [CrossRef]
94. Yang, J.H.; Wu, F.Y.; Chung, S.L.; Lo, C.H. The extensional geodynamic setting of Early Cretaceous granitic intrusions in the eastern North China Craton: Evidence from laser ablation 40Ar/39Ar dating of K-bearing minerals. *Acta Petrol. Sin.* **2008**, *24*, 1175–1184. (In Chinese with English abstract)
95. Yang, J.H.; Wu, F.Y.; Wilde, S.A.; Chen, F.; Liu, X.M.; Xie, L.W. Petrogenesis of an alkali Syenite-Granite-Rhyolite suite in the Yanshan Fold and Thrust Belt, Eastern North China Craton: Geochronological, geochemical and Nd-Sr-Hf isotopic evidence for lithospheric thinning. *J. Petrol.* **2008**, *49*, 315–351. [CrossRef]
96. Lin, W.; Faure, M.; Monie, P.; Scharer, U.; Panis, D. Mesozoic extensional tectonics in eastern Asia: The south Liaodong Peninsula metamorphic core complex (NE China). *J. Geol.* **2008**, *116*, 134–154. [CrossRef]

97. Liu, J.L.; Shen, L.; Ji, M.; Guan, H.M.; Zhang, Z.C.; Zhao, Z.D. The Liaonan/Wanfu metamorphic core complexes in the Liaodong Peninsula: Two stages of exhumation and constraints on the destruction of the North China Craton. *Tectonics* **2013**, *32*, 1121–1141. [CrossRef]
98. Davidson, J.P.; Morgan, D.J.; Charlier, B.L.A.; Harlou, R.; Hora, J.M. Microsampling and isotopic analysis of igneous rocks: Implications for the study of magmatic systems. *Annu. Rev. Earth Planet. Sci.* **2007**, *35*, 273–311. [CrossRef]

Disclaimer/Publisher's Note: The statements, opinions and data contained in all publications are solely those of the individual author(s) and contributor(s) and not of MDPI and/or the editor(s). MDPI and/or the editor(s) disclaim responsibility for any injury to people or property resulting from any ideas, methods, instructions or products referred to in the content.